FULL PAPERS

Magnetic Resonance in Medicine 000:000–000 (2011)

Thalamus Segmentation Based on the Local Diffusion Direction: A Group Study

Sarah C. Mang,[1,2]* Ania Busza,[1,3] Susanne Reiterer,[1] Wolfgang Grodd,[1,4] and Uwe Klose[1,5]

Fast and accurate segmentation of deep gray matter regions in the brain is important for clinical applications such as surgical planning for the placement of deep brain stimulation implants. Mapping anatomy from stereotactic atlases to patient data is problematic because of individual differences in subject anatomy that are not accounted for by commonly used atlases. We present a segmentation method for individual subject diffusion tensor MR data that is based on local diffusion information to identify subregions of the thalamus. We show the correspondence of our segmentation results to anatomy by comparison with stereotactic atlas data. Importantly, we verify the consistency of our segmentation by evaluating the method on 63 healthy volunteers. Our method is fast, reliable, and independent of any segmentation before the classification of regions within the thalamus. It should, therefore, be useful in clinical applications. Magn Reson Med 000:000–000, 2011. © 2011 Wiley-Liss, Inc.

Key words: segmentation; DTI; thalamus; validation

Many illnesses, including Parkinson's disease, schizophrenia, and chronic pain syndrome, are associated with changes in the thalamus (1–4). Dissection or stimulation of certain regions in the thalamus can reduce symptoms of some of these illnesses (5,6). Currently, surgical planning is based on MR imaging and anatomical predictions created by mapping a stereotactic brain atlas onto visually identifiable landmarks in the patient's brain (7). However, anatomical variability of deep gray matter structures relative to currently used atlases can make such techniques challenging (8). Therefore, development of more accurate and efficient segmentation techniques for deep gray matter regions, such as the thalamus, is of increasing clinical importance. Unfortunately, the thalamus has a mostly homogeneous signal value in standard anatomical MR images (see Fig. 1a). Segmentation of thalamic nuclei is therefore not possible on these kinds of data sets. Although some substructures of the thalamus are visible on higher resolution anatomical MR images or magnetization transfer images (see for example (9–11)), high-resolution imaging also increases the measurement time, which is a disadvantage for clinical applications. Deoni et al. (9) successfully used modified k-means clustering to segment thalamic nuclei in high-resolution quantitative MR images. The results of this method were very promising, however the technique required manual segmentation of the whole thalamus and prior information from stereotactic atlases (12) to reduce the computational cost of the segmentation.

Other approaches use diffusion tensor MR-imaging (DTI) to segment individual regions in the thalamus. DTI measures the direction of water molecular diffusion to detect the dominant orientation of fibers in living tissue (for details on DTI see for example (13,14)). It therefore has a high potential to be useful in the segmentation of the thalamus because individual thalamic nuclei have well-structured fiber connections to defined cortical and subcortical areas. Figure 1b shows an example of how diffusion information can aid in distinguishing thalamic substructures. Indeed, there have been several reports of new thalamus segmentation techniques using DTI technology in recent years (15–21).

The methods proposed by Wiegell et al. (19) and Ziyan et al. (20,21) use clustering methods to find an optimal subdivision of the thalamus. In this approach, the number of clusters to be segmented is predefined, and the voxels are automatically assigned to the individual clusters according to local diffusion tensor information similarity and spatial proximity. The segmentation quality of these methods depends to a large part on the number of clusters that is chosen by the user and the quality of the manual segmentation of the whole thalamus before the application of the clustering algorithms.

The segmentation method proposed by Behrens et al. (15,17) uses connectivity to cortical areas to distinguish between individual regions in the thalamus. This approach requires manual segmentation of the cortical regions as well as extensive fiber tracking. The results are reliable but require considerable computation time. They depend on both the quality of the initial manual segmentation and the quality of fiber tracking. The level of detail of the parcellation depends on the number of presegmented cortical regions, which corresponds to the number of regions that will be identified in the thalamus. An improved version of the connectivity-based segmentation by Jbabdi et al. (16) does not require the user to pre-emptively define the number of thalamic subdivisions. This method can show segmentation quality similar to that of the original method by Behrens et al. (15) but is still very sensitive to user-defined parameters in the model used for the segmentation.

[1]Previous "Section for Experimental MR of the CNS," Department of Diagnostic and Interventional Neuroradiology, University Hospital Tuebingen, Germany
[2]Software Development for Integrated Diagnostics and Therapy, German Cancer Research Center, Heidelberg, Germany
[3]MD/PhD Program, University of Massachusetts Medical School, Worcester, Massachusetts, USA
[4]Department of Psychiatry, Psychotherapy and Psychosomatics, University Hospital Aachen, Germany
[5]MR Research Group, Department of Diagnostic and Interventional Neuroradiology, University Hospital Tuebingen, Germany
*Correspondence to: Dr. Sarah Mang, Software development for Integrated Diagnostic and Therapy (SIDT), German Cancer Research Center (E071), Im Neuenheimer Feld 280, D-69120 Heidelberg, Germany. E-mail: s.mang@dkfz-heidelberg.de

Received 8 September 2010; revised 11 April 2011; accepted 14 April 2011.
DOI 10.1002/mrm.22996
Published online in Wiley Online Library (wileyonlinelibrary.com).

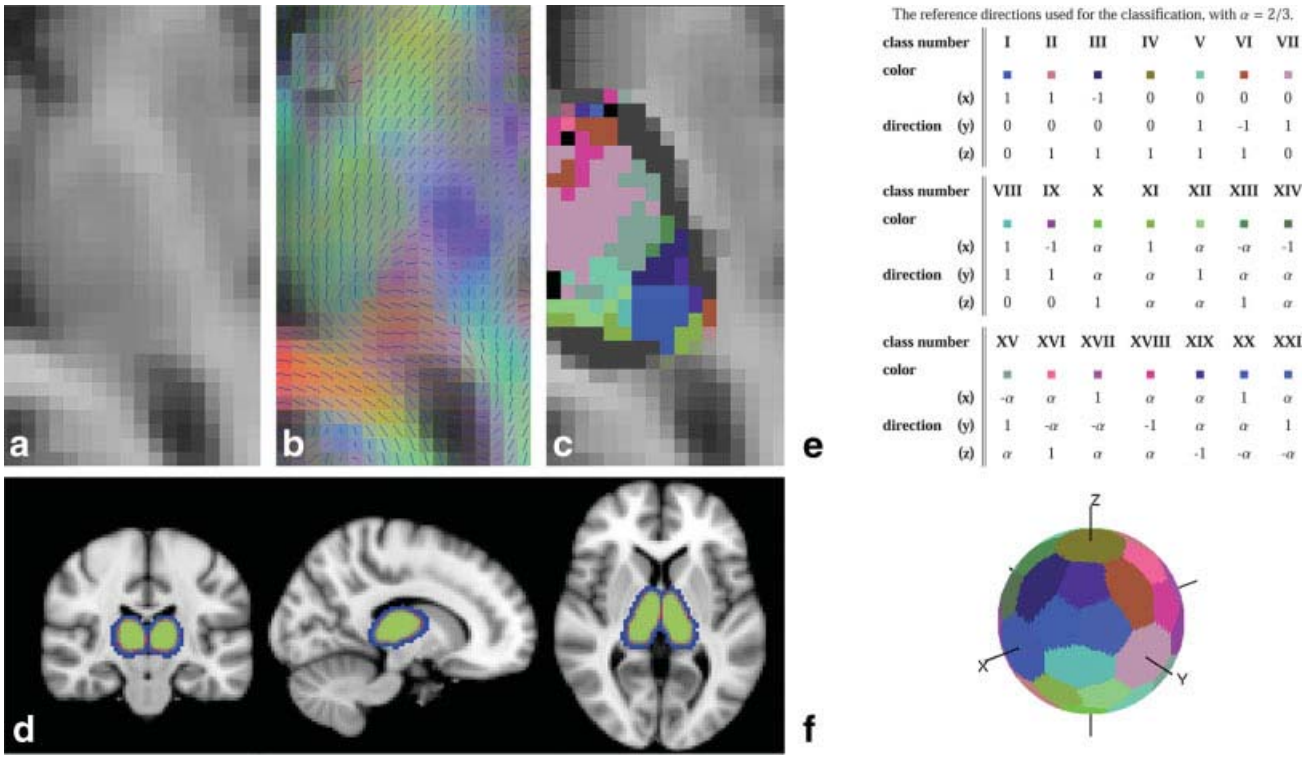

FIG. 1. DTI Segmentation. **a**: T_1-weighted axial image of the thalamus showing weak intrinsic contrast, which prevents a detailed distinction of thalamic substructures. **b**: DDO overlayed on a color-coded FA map demonstrating the enhanced intrinsic contrast (color maps the DDO to RGB space). **c**: Unique color coding of the DOCs segmentation using the orientation-dependent coloring as defined in (f). The shape of structures in digital atlases depends on the applied probability threshold and the atlas used. **d**: shows the difference between the thalamus masks given by the Harvard-Oxford subcortical structural atlas taken from FSL (22) with a minimal probability of 5% (in dark to light blue) and 50% (overlayed in red to yellow). For the visualization of our results, we chose a mask with at least 50% probability from the Harvard-Oxford sub-cortical structural atlas. **e**: gives the reference directions for the 21 DOCs and the corresponding color coding. The distributions of the DOCs over the unit-sphere is shown in (**f**), where the centroids of the color-patches correspond to the reference directions.

The method proposed by Unrath et al. (18) uses only the principal diffusion direction, presumably corresponding to the local fiber orientation, for the identification of thalamic subregions. This diffusion-direction-based method is a simple and fast segmentation technique. In contrast to the DTI-based methods previously described, classification techniques based on the principal diffusion direction are much less sensitive to user-defined parameters and do not rely on prior manual segmentation. The segmentation method described by Unrath and colleagues is able to resolve large thalamic sub-regions and therefore is potentially useful in clinical settings.

Here, we present an adapted version of the segmentation method presented by Unrath et al. As opposed to Unrath and colleagues, who grouped their reference orientations into nine segmentation classes, we use the full set of 21 reference orientations for a more detailed segmentation. We evaluate our adapted segmentation method on 63 healthy subjects and show that the resulting segmentation corresponds well with known anatomical structures of the thalamus, both in a group average and in individual subjects. Furthermore, an evaluation of the center-of-mass (COM) for different thalamic substructures identified by our technique and probability maps for these substructures shows that the segmentation results of individual subjects are spatially consistent. Our results suggest that segmentation based on the dominant diffusion direction consistently identifies substructures of the thalamus and, therefore, may be useful in clinical settings.

MATERIALS AND METHODS

Subject Group and Data Acquisition

Data for the presented investigations were collected from 63 healthy right-handed volunteers (32 males and 31 females) between 20 and 40 years of age (mean 26.29 years $\pm$ 4.84, females mean 25.52 years $\pm$ 4.35), originally recruited for a nonassociated study. All subjects gave written informed consent to the data acquisition and its evaluation for research purposes.

T_1-weighted anatomical images and DTI data were acquired on a 1.5-T MR Scanner (Sonata, Siemens, Erlangen, Germany). The T_1-weighted images were acquired with a modified driven-equilibrium Fourier transform sequence with a TR of 7.92 ms, TE of 2.48 ms, and a voxel size of 1 mm^3. The DTI measurement included 12 diffusion-weighted images (DWI) and an unweighted image for each subject with the standard Siemens sequence covering the whole brain with a b-value of 800 s/mm^2 (TR = 6700 ms

and TE = 82 ms). The in-plane resolution for the DTI data was $2 \times 2\,mm^2$, the slice thickness 2.5 mm.

Preprocessing

For automated comparison of the individual subject data, all data sets were aligned, interpolated to $2\,mm^3$ isotropic resolution, and normalized to the MNI152 template ($2\,mm^3$) from the FMRIB Software Library (FSL) (22). First, the T_1-weighted anatomy image was aligned with the MNI template using the "flirt" routine in FSL. Then, an affine transformation (flirt from FSL) was used to match the individual diffusion-weighted images to the anatomy. This step also compensated for motion during the DWI acquisition. The corresponding gradient directions were adapted accordingly (23–25). The tensor was then estimated from the aligned data using the "analyzedti" function from Camino (26). Then, a nonlinear warp was applied to normalize the anatomy image to the MNI template (fnirt function from the FSL library). This transformation was also applied to all individual tensor elements. Finally, the orientation of the tensors was corrected using the "reorient" routine from the Camino library (23,26) before the dominant diffusion orientations (DDOs) were extracted from these tensors.

Segmentation and Creation of Individual Classification Maps

The segmentation method used in our group evaluation is an adaptation of a previously presented segmentation method that is based on the classification of local DDOs (18,27). For each voxel, the DDO is computed by diagonalization of the second-order diffusion tensor. It is assumed to be equal to the eigenvector corresponding to the largest eigenvalue. The direction of the diffusion process determined from DTI data is presumably symmetric, i.e., equal in either direction on an orientation axis. Therefore, we refer to DDOs and not directions. Example DDOs are illustrated in Fig. 1b as lines.

To identify thalamic areas with similar DDOs, we use a set of predefined reference orientations (Fig. 1e and f) to classify every voxel in a data set based on similarity between reference orientations and local DDOs. We did use the set of reference directions proposed by Unrath et al. (18). Each reference direction defines a diffusion orientation class (DOC) as shown in Fig. 1e. To construct the set of reference directions first the three main axes (class I, IV, and VII) are used. They define the octants of the unit sphere that were used as basis for the subdivision of the sphere proposed by Unrath et al. This can also be appreciated on the color-sphere representation of the DOCs in Fig. 1f. Each octant has a similar subdivision into nine regions. Beside the three main axes each octant has three reference directions consisting of a mixture of two of the main axes (*xy*—VIII, IX; *xz*—II, III; *yz*—V, VI) and three reference directions mixing all three axes (class X–XXI). This results in a total of 21 DOCs. In the classification step, each voxel is assigned the DOC whose reference orientation r has the least angular difference d from the voxel's local DDO,

$$d(i) = \arccos(|\overleftarrow{r_i} \cdot \overleftarrow{\mathrm{DDO}}|). \quad [1]$$

If the classification should not be unique, that is, a local DDO has the same minimal angular difference to several reference orientations, the voxel is assigned the first class with minimal angular difference. A more detailed discussion on nonunique classification can be found in the sections on partial-volume-effects.

For visual clarity, each DOC is displayed using a distinct, unique color from the color-coding proposed by Demiralp et al. (28). Each defined class along with its corresponding color and reference orientation is given in Fig. 1e. DDOs are assigned to the DOC into whose color patch they are projected on the sphere depicted in Fig. 1f. The reference orientations correspond to the centroids of each color patch on the displayed unit-sphere.

We called the complete segmentation results of a single subject, where each voxel is displayed in the color of the corresponding DOC, an "Individual Classification Map" (ICM). An example of an ICM is given in Fig. 1c. In an ICM, there are connected regions consisting of neighboring voxels that are assigned the same DOC. These connected regions for the individual DOCs, which will be segmented, are called "clusters."

Evaluating the Intersubject Consistency

If individual clusters are spatially similar in the ICMs, then the locations of their COMs would also be similar. Therefore, we evaluated the COMs for the main clusters in the ICM to investigate the intersubject consistency of our ICMs. To calculate the COM, we used:

$$\mathrm{COM} = \frac{1}{|\Omega|} \sum_{i \in \Omega} \overleftarrow{a_i}, \quad [2]$$

where $|\Omega|$ is the number of voxels in the cluster Ω, and $\overleftarrow{a_i}$ is the position of the ith voxel inside the cluster.

To restrict the COM evaluation to clusters that are most certainly located inside the thalamus, the probability mask from the Harvard-Oxford subcortical structural atlas (22) was thresholded to contain only voxels that were inside the thalamus with a probability above 50% (see Fig. 1d). The mask is applied after classification and, therefore, does not affect this step of the segmentation process. The individual segmented clusters do not exceed the applied mask, their borders might therefore be restricted by this mask.

Group Results in Comparison with Anatomy and Stereotactic Atlas Data

Two kinds of group summaries were defined for comparison with higher resolution T_1 images and atlas data. First, we defined probability maps that show the overlap of corresponding ICM clusters in all subjects. If the probability is 100% in a voxel, this voxel is similarly classified in all 63 evaluated subjects. Second, we summarized the segmentation results from individual subjects into a "Dominant Classification Map" (DCM) for the entire subject group. In this map, each voxel is assigned the DOC that occurred most often in the corresponding voxel in individual subjects. The DCM allows no overlap between the displayed clusters, unlike the probability maps.

Multiple slices in all three planes (sagittal, horizontal, and coronal) of the DCM were visually compared with the corresponding T_1 slices taken from the template brain (1-mm isotropic voxel resolution) provided by FSL (22). A lower resolution version (2-mm isotropic voxel resolution) of this template was used in the preprocessing of the data. Similar slices from the probability maps were compared with corresponding slides in the histological atlas (12) to determine the correspondence of our segmentation results to the anatomy presented in the atlas.

Partial-Voluming Effects

The discrete voxel resolution that is intrinsic to any MR-imaging method does not allow the distinction between pure gray matter and pure white matter in the thalamus on our DTI data sets. A number of voxels will contain both matter types, independent of the image resolution. This is not a problem for our segmentation method, because gray matter is believed to have an isotropic diffusion profile. The gray matter part of a voxel will therefore reduce the FA but will not affect the orientation of the DDO, on which our segmentation is based.

Some voxels on the surface of the thalamus may contain areas of neighboring cerebrospinal fluid (CSF) or fiber bundles. As our segmentation approach uses the DDO of a voxel for its classification, voxels comprised of mixed thalamus/CSF or thalamus/external fiber bundles could potentially interfere with our segmentation results. We used FA value restrictions to exclude voxels that might be affected by so-called "partial-voluming-effects" from our analysis.

CSF is assumed to have an isotropic diffusion profile, because the diffusion in the ventricles is not hindered by closely packed anatomical boundaries such as neuronal fibers or cell bodies. A voxel that partially consists of CSF will therefore have a lower fractional anisotropy (FA) value than a voxel containing only thalamic structures. We assume that the thalamic component in a voxel is larger than the CSF component if its FA value is above 0.1. Such voxels are therefore used in our segmentation. The thalamus also borders on larger fiber bundles with high FA values. The FA of these bundles is considerably higher than in the thalamus, where the FA is reduced by an inseparable mixture of gray and white matter. We chose an upper FA threshold of 0.5 to ensure that the thalamic component of a voxel with lower FA value outweighs the part containing high-FA-valued fiber bundles.

On the border between thalamic subregions voxels may contain parts of different thalamic substructures with different fiber orientations. This may cause the local DDO to lie between DOCs. The classification in this case is not unique, because the angular difference between the DDO and more than one reference orientation is minimal. In our evaluation of nonunique classification, we did assume that the angular difference between a local DDO and the reference orientations was similar if it deviated less than 1°. We evaluated how this case of partial-voluming affects our segmentation results by investigating the number of affected voxels and their location.

Table 1
The center-of-mass (COM) for the Individual Clusters in the Right Thalamus Is Given for the Anatomically Most Relevant Clusters in MNI Coordinates (in mm).

		Mean (COM)			Avg (dev)	Std
Cluster	Class	*x*	*y*	*z*	(mm)	(mm)
1	I	16.20	−30.06	4.14	1.10	0.66
2	II	19.72	−33.34	2.46	1.78	1.24
3	III	17.82	−23.04	4.94	1.48	0.70
4	VI	1.28	−7.50	9.20	1.72	1.14
5	VII	0.74	−14.78	8.52	0.86	0.56
6	XIII	11.96	−22.78	4.68	2.40	1.68
7	XIV	14.56	−19.64	2.66	2.30	1.32
8	XV	11.92	−15.81	7.26	2.32	1.54

To appreciate the similarity of the COMs for a certain DOC in individual subjects the average deviation (avg(dev)) of the individual COMs from the mean(COM) and the corresponding standard deviation (std) are given in mm.

Correction of Corrupted DDOs

Sorting bias is the result of noise and affects voxels randomly by interchanging the diffusion directions (29), which could result in false orientation classifications in our segmentation approach. Also randomization in the sorting of eigenvalues in spherical diffusion tensors may affect the classification. Common methods to reduce corrupted DDOs use neighborhood information (30,31). Although these neighborhood-based methods are not able to completely eliminate error in the reconstructed DDOs, they can decrease it considerably.

Here, we used our group data set to assess the effect of corrupted DDOs on our segmentation results. We checked each ICM voxel that had a DOC different from the DOC calculated for the group DCM for corrupted DDOs. For each of these voxels, the DOC for the minor diffusion directions was determined and compared with the DOC of the DCM. If one of the minor DOCs matched the one in the group DCM, then the order of the eigenvectors for the voxel was corrected accordingly. The number of voxels that were affected by corrupted DDOs and the number of subjects whose voxels need correction were used to assess the overall effect of corrupted DDOs.

RESULTS

Evaluating the Intersubject Consistency

In the presented evaluations, we concentrate on relatively large clusters, which are consistently positioned in over 50% of our subjects. We therefore focus our investigations on the clusters for DOCs I, II, III, VI, VII, XIII, XIV, and XV, whose mean size over all ICMs is larger than 20 connected voxels. For easier handling, the clusters are numbered from 1 to 8 as defined in Table 1.

The individual ICMs of the 63 evaluated subjects correspond very well to each other. This is illustrated in Fig. 2b, where the COMs of these eight clusters are shown for all subjects. The COMs for each individual DOC lie close together, showing the consistent placement of the clusters in the individual ICMs.

A quantitative assessment of the consistency is given in Table 1, where the position of the mean COM over all

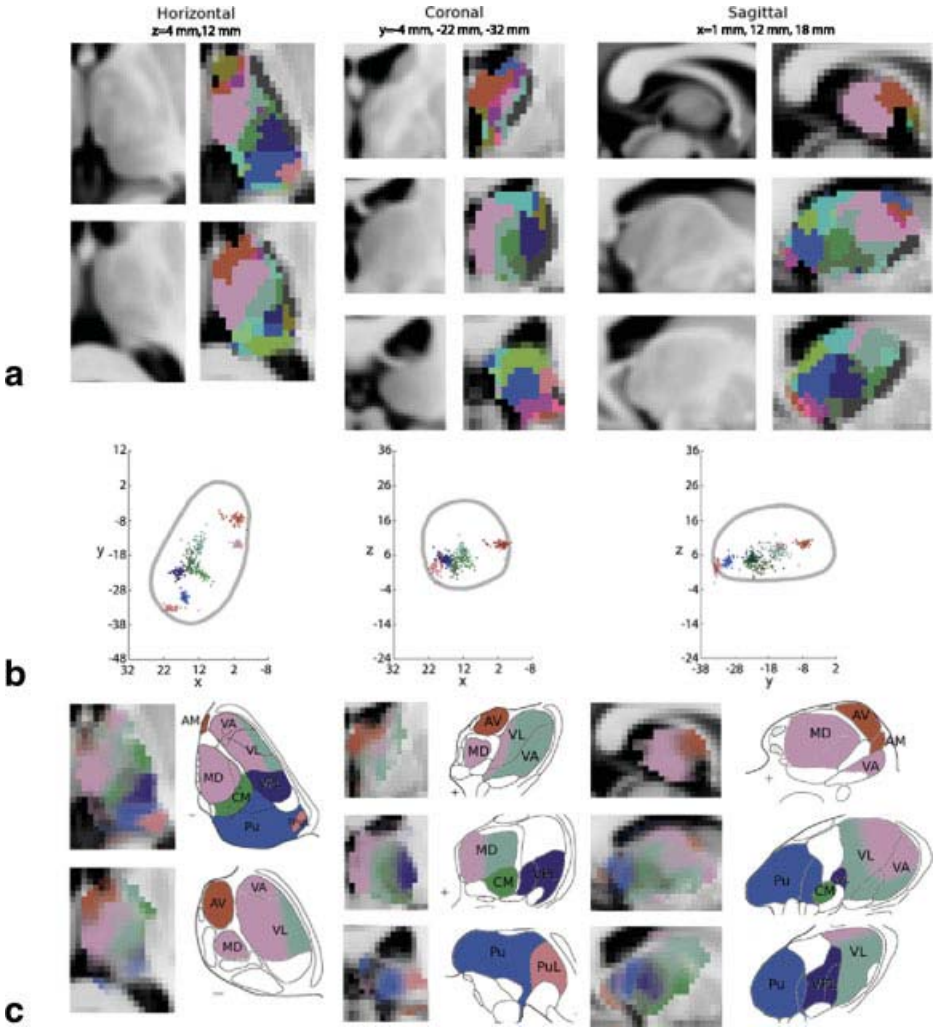

FIG. 2. The results are shown for several slices through the thalamus—the coordinates at the top are given in MNI space. **a**: the Dominant Classification Map (DCM) illustrates the results of our DTI segmentation method from our entire subject group. For anatomical comparison, the corresponding thalamic slices from the reference brain (22) with 1-mm isotropic resolution are also presented. **b**: COM coordinates for major DOCs show strong intersubject consistency in location. Each dot corresponds to the COM of a DOC cluster from one subject. Scatter-plots of all individual COMs for each of the major DOCs are shown. A schematic outline of the thalamus is included on each plane for spatial reference. For better identification the color-coding of the COMs corresponds to that of the DOCs presented in Fig. 1. **c**: the probability maps of the eight large clusters are given on the left. The displayed probabilities are restricted to the interval between 50% (fade out) and 100% (opaque). The colors match the corresponding DOC. The corresponding slides from Morel's atlas (12) are given on the right and are colored to correspond the DOCs (slide number top/down: Horizontal: D4.5, D10.8; Coronal: P1.8, A7.2, A18; Sagittal: L5.4, L11.7, L16.7).

subjects is given for each cluster. The consistency can be appreciated by comparing the average deviation (avg(dev)) of the individual subject COMs from the mean COM for each cluster and the corresponding standard deviation (std).

The grouping of the COMs is especially tight for the clusters that were discussed in the original work by Unrath et al. (18), the lateral group (cluster 1 in blue), the frontal group (cluster 5 in lilac), and the parietal group (cluster 2 in dark rose and cluster 3 in dark blue). The average deviation from the mean COM for these clusters is smaller than the voxel size (less than 2 mm). The corresponding standard deviation is also very small (see Table 1).

The COM for cluster 4 in brown also shows very good intersubject correspondence with a mean deviation smaller than the voxel size (2 mm), even though the cluster is much smaller in size than the previously discussed ones. The COMs for cluster 6 in dark green, cluster 7 in hunter green, and cluster 8 in gray green are slightly wider spread but still correspond well between subjects. Their average deviation from the mean COM of the cluster was slightly larger than the voxel size of 2 mm (see Table 1), but the corresponding standard deviation is sufficiently low.

Comparison between Probability Maps and Stereotactic Atlas

Figure 2c shows selected slices in horizontal, sagittal, and coronal orientation through the probability maps of the eight largest clusters in our results and corresponding

slides from a well-known multiarchitectonic/stereotactic atlas (12). The opacity of the probability maps indicates the probability value. Completely opaque is equal to 100% probability. The maps fade out when the probability for a cluster drops beneath 50%. All the eight presented clusters have large core-regions with probability values above 90%.

Through visual comparison of the cross sections of the probability maps with atlas data (12), we identified the major thalamic nuclei associated with each cluster. Our observations are as follows: cluster 1 (DOC I; blue) consists of a large portion of the caudal thalamus. It is slightly more dorsomedially situated and includes most of the posterior protrusion of the thalamus. We therefore conclude that cluster 1 corresponds well with the pulvinar nucleus (Pu), and the medial pulvinar in particular. Cluster 2 (DOC II; dark rose) is also caudally located and consists of a smaller area lateral to cluster 1. This area is consistent with the location of the lateral pulvinar nucleus (PuL). Cluster 3 (DOC III; dark blue) is a larger cluster situated laterally along the outer shell of the thalamus. It is anterior to the pulvinar clusters (clusters 1 and 2) and correlates well with the location of the ventral posterior lateral nuclei (VPL). Other ventral posterior nuclei, such as the ventral posteromedial or the ventral medial nuclei, may also be part of cluster 3. However, the small size of these nuclei make it difficult to determine their exact location within our DOC clusters. Cluster 4 (DOC VI; brown) is our anterior-most cluster. It consists of a dorsal area of the thalamus that bulges out into the lateral ventricle, an area comprising the anterior group of the dorsal thalamic nuclei, including the anteroventral nucleus (AV) and likely the anterodorsal and anteromedial nuclei as well. Cluster 5 (DOC VII; lilac) is a large area comprising most of the medial thalamus. In combination with cluster 8 (DOC XV; grey green), these clusters include the thalamic area corresponding to the medial dorsal nucleus (MD) medially and ventral lateral nuclei (VL) and ventral anterior nuclei (VA) laterally. Clusters 6 (DOC XIII; dark green) and 7 (DOC XIV; hunter green) are smaller clusters that show high consistency. Cluster 6 is anatomically consistent with the location of the central median nucleus (CM). Cluster 7 appears briefly in several sagittal sections but does not correlate consistently with any well-described anatomical subdivisions. We wonder if it may be part of fiber bundles crossing at the lateral edge of the thalamus. This described correspondence between known thalamic anatomy and our segmentation classes is illustrated by corresponding coloring of the atlas slides in Fig. 2c.

Evaluation of the DCM

The clusters presented in the DCM (Fig. 2a) do not overlap and are not weighted according to their intersubject correspondence as opposed to the ones presented in the probability maps (Fig. 2c). A comparison between the probability maps and the DCM shows that the eight clusters from the probability maps cover the largest part of the DCM. The core regions of the eight clusters in the probability maps with high probability match the corresponding clusters in the DCM well.

Some of the larger clusters in the DCM are not included in the probability maps. The clusters of DOC IV show probably part of the fornix and the capsula interna (dark ocher in Fig. 2a). Therefore, it was excluded from the probability maps even though it has high probability values. The clusters for DOC VIII (turquoise) and DOC XI (pear) have only a small high-probability core region (less than 10 connected voxels with a probability value above 80%) and were therefore not included in the group of major clusters. These clusters seem to be more sensitive to imperfections in the normalization, which will reduce the intersubject correspondence and therefore the probability values. This may also be due to their placement on a border between CSF and the thalamus. These clusters might still represent anatomically relevant regions and need to be investigated further. Other clusters in the DCM that were not included in the probability maps are small and therefore more variable than the larger clusters. Their high-probability core is reduced to individual voxels or small voxel groups (less than five connected voxels with a probability value above 80%). The probability values of small clusters are more sensitive to imperfect normalization because of the smaller possible overlap of the clusters between subjects.

A comparison of the DCM with the higher resolution anatomical images (Fig. 2a) shows that our segmentation results correspond well with structures that are visually detectable in the anatomical images, such as the pulvinar nucleus (in blue). The border between the pulvinar nucleus and the ventral posterior lateral nuclei (dark blue) can be appreciated especially well in the horizontal cut at 4 mm and the sagittal cut at 18 mm. In the sagittal cut at 1 mm and the horizontal cut at 12 mm, the visually detectable border between medial dorsal nucleus (lilac) and the anterior nuclei (brown) is spatially correspondent to the border in the DCM.

Partial-Voluming Effects

We evaluated how nonunique classification affects our segmentation results. We found that ~3% of the voxels in the ICMs was affected by nonunique classification. Most of the affected voxels were assigned to two DOCs. Approximately 3% of the nonuniquely classified voxels were assigned to three DOCs. No voxel was assigned to more than three DOCs. The relative number of affected voxels was independent of thresholding of the applied thalamus mask. All affected voxels were isolated and mostly located on the border between clusters. No connected subclusters were affected. Also, we could find no consistent placement of these nonuniquely classified voxels within our subject group. A single voxel position showed the maximum of nine subjects (<15%) with nonunique classification. The average number of subjects for nonuniquely classified voxels was 2.35 (std = 1.42), which is less than 4% of the subjects. The effect of nonunique classification was not considered to significantly affect the segmentation results. Voxels with nonunique classification were, therefore, not handled in a special way.

Correction of Corrupted DDOs

We investigated whether our segmentation results are affected by corrupted DDOs. We found that only individual voxels but no connected subregions of segmented clusters

are affected by corrupted DDOs. Less than 1% of the voxels in each subject are affected. For these individual voxels, a maximum of three subjects inside the masked thalamus were biased, which is less than 6% of the subjects.

We also investigated the effect of corrupted DDOs if only voxels with a probability greater than 50% were considered for the DCM. In these voxels, one can assume that the classification in the DCM is likely accurate because randomness would cause probability values below 50% in a large subject population with 21 segmentation classes. The results were similar to the evaluation of corrupted DDOs without probability thresholding. The effect of corrupted DDOs was, therefore, considered to be negligible. No correction was applied to the data presented here.

DISCUSSION

We have developed an alternate DTI-based thalamus mapping protocol, which is fast, reliable, more detailed than previously reported segmentation methods, and independent of manual segmentation. Although small thalamic subregions are not detectable with our method because of coarse image resolution and resulting partial volume effects, larger subregions can be identified consistently in a large number of subjects.

The computation time for our segmentation method is very short. The required preprocessing was done in a few minutes per subject on a standard processor. The segmentation of preprocessed DTI data required only a few seconds in our reference implementation.

Our segmentation method is much faster than the connectivity-based method proposed by Behrens et al. (15,32), because no fiber tracking is required. It also avoids the problems of the used tracking algorithm, such as accumulated noise effects along the reconstructed tract, or the effect of tract termination criteria on the reconstructed connectivity.

Additionally, unlike a connectivity-based approach, our method can in theory identify thalamic subregions that do not have a direct connection to the cortex. This is important because the thalamus consists of two kinds of nuclei: specific nuclei, which have a direct connection to well-defined cortical regions, and unspecific nuclei, which are not directly connected to the cortex but have indirect connections through other (specific) nuclei. Previously described connectivity-based methods (15–17) cannot separate the unspecific nuclei from the specific ones they are connected with. Our segmentation method does not necessarily group unspecific nuclei in the thalamus with the specific nuclei they are connected with. Only local diffusion information is evaluated in our segmentation approach. A remaining difficulty with identifying unspecific nuclei is that they are usually very small and therefore cannot be resolved in data sets with a voxel resolution as coarse as the one in the data evaluated here. Improvement in image acquisition will likely lead to improved voxel resolution in the future and may allow for accurate identification of unspecific thalamic nuclei with our method.

The presented segmentation method does not require any manual interaction. The masks and FA-thresholds applied to the presented data are only used after the classification of all voxels. They help focusing the visualization of the segmentation results on the thalamus by excluding structures bordering on the thalamus. The masks and thresholds do not affect the actual classification results. In contrast, the previously presented DTI-based segmentation methods (9,15,19–21,32) all require segmentation of the whole thalamus before the segmentation of thalamic substructures. Especially in clustering-based segmentation methods, the segmentation of the whole thalamus will not only influence the segmentation of the individual subthalamic regions but also affect the classification process. Clustering methods do not only consider local features but also spatial proximity of the voxels that are classified. Voxels neighboring a specific cluster might be added to this cluster if spatial proximity outweighs the feature part. The connectivity-based thalamic subdivision (15,32) uses only the connectivity of the individual voxels to classify the voxels within the thalamus for the segmentation. The size of the manually segmented thalamus mask will affect the time required for the segmentation, because every voxel within the thalamus mask will be processed in the time-consuming fiber-tracking. The accuracy of the segmentation of cortical target regions will affect the classification of the voxels within the thalamus. Manual segmentation is subjective and dependent on the individual that defines it. Therefore, it adds another cause for variability to the results.

To reduce the variability in the results and increase their reproducibility, the segmentation of the thalamus or cortical regions could also be acquired from digital atlases. The contours taken from probabilistic atlases such as the Harvard-Oxford subcortical structural atlas (22) depend on the selected threshold applied to the probability. The difference in the contours between a minimal probability of 5 and 50% can be appreciated in Fig. 1d. The contours of structures taken from different atlases with the same probability may also deviate considerably. Even though the use of atlases reduces the variability in the segmentation, the differences in the contours taken from the atlases will influence the results of the thalamus segmentation as discussed in the previous paragraph. This will hinder inter-study comparison, if the exact same parameters were not used to determine the contour of the whole thalamus and the required cortical regions.

Our segmentation shows more detail than the method proposed by Unrath et al. (18), because we use 21 distinct DOCs instead of combining the 21 reference orientations to 9 DOCs. Our 21 DOCs can be translated into the DOCs used by Unrath et al. by combining the major-diagonal DOCs II and III, DOCs V and VI, and DOCs VIII and IX, and combining the minor-diagonal DOCs (X-XXI) into groups of four ({X, XIII, XVI, XIX}, {XI, XIV, XVII, XX}, {XII, XV, XVIII, XXI}). This reductionist method has several useful features. It allows for easier appreciation of interhemispheric symmetries, because symmetric clusters now belong to a single DOC. In our approach, the symmetry problem could be handled by inverting the corresponding reference orientations, i.e., using a mirrored color sphere or mirrored reference orientations for one hemisphere to ensure that symmetric clusters of the two hemispheres belong to the same DOC in our segmentation. The most prominent advantage in using 21 DOCs is the distinction between clusters 2 (DOC II; dark rose) and 3 (DOC III; dark blue) as shown in Fig. 2.

These two prominent clusters were grouped together in the classification with nine DOCs (18).

A reason why Unrath et al. may not have considered some of the clusters that we present is their small size in comparison with the size of the three dominant clusters they presented. The greater number of DOCs in our method as well as the large size of our subject group and improved data quality allowed us to identify additional clusters, even if they are relatively small. For example, cluster 4 (DOC VI; brown), which shows very low mean deviation (less than a voxel) in the COM of the individual subjects. The large number of subjects that show corresponding clusters in the same position after normalization suggests that even small clusters represent anatomically meaningful areas, which could not be appreciated well on the nine subjects investigated by Unrath and colleagues.

The inter-subject agreement of COMs for individual clusters demonstrates that the segmentation results from individual subjects correspond well to each other. The results can therefore be called reliable. Even smaller clusters, such as clusters 4, 6, 7, and 8, that have not been presented previously have a good interindividual consistency, and therefore, we believe them to be anatomically relevant.

The similarity of our segmentation results to anatomy from a classic stereotactic atlas (12) is shown in Fig. 2c. The DCM and probability maps, summarizing the results from all 63 individuals in our subject group, corresponds well to previously described anatomy as shown in Fig. 2.

The speed in which our segmentation is done (a few seconds on preprocessed DTI data; preprocessing requires a few minutes) permits its application in clinical context. As our method does not require user interaction, the segmentation can be computed without supervision for later evaluation by experts.

Ziyan et al. evaluated several metrics on DTI data for their spectral clustering (20). They found that angular difference between DDOs produces the best segmentation results. This supports our choice to use angular difference for the classification step in our segmentation.

Our method is based solely on the dominant diffusion direction and could, therefore, be affected by DDOs corrupted due to noise or random errors on spherical diffusion tensors. As our investigations found that only a small number of individual voxels are affected by the corrupted DDOs, we believe the effect on the final result is negligible. Therefore, we did not include a correction for corrupted DDOs in our protocol.

In our classification, DDOs that have a similar minimal angular difference to more than one reference orientation are not handled separately. We found that nonunique classification affected our segmentation results only marginally. Voxels with nonunique classification were therefore not processed differently from uniquely classified voxels.

To extend the work by Unrath et al. (18) in our investigations, we used the same set of reference orientations. These reference orientations are neither equiangular nor equidistant on the surface of the unit sphere. Improving the tessellation of the unit-sphere described by the reference orientations may improve the segmentation results. A different approach for improving the set of reference orientations is not based on a geometrical tessellation of the unit sphere but considers fiber orientations from anatomy. The borders of the segmented clusters could possibly be improved if the reference orientations were chosen based on anatomy. The optimization of the reference orientations and the effect of this optimization are the topic of future investigations. However, the consistency of the segmentation between individual subjects and the correspondence of our segmented clusters with previously identified nuclei suggests that our geometrical distribution of reference orientations is already a good approximation of reference orientations based on anatomy.

Our segmentation method can be applied to any fibrous structure, which means it is not restricted to the thalamus. The usability of our segmentation approach for other regions in the brain is under investigation.

CONCLUSIONS

On the basis of the local DDOs. The segmented clusters show good intersubject consistency in normalized data sets of a large subject population. The method is very fast and independent of segmentation of any kind before the subdivision of the thalamus. Therefore, we believe our method may prove to be useful in clinical applications.

ACKNOWLEDGMENTS

The authors thank Dr. Esra Gurdal for her guidance in anatomical validation of our results.

REFERENCES

1. Byne W, Buchsbaum MS, Mattiace LA, Hazlett EA, Kemether E, Elhakem SL, Purohit DP, Haroutunian V, Jones L. Postmortem assessment of thalamic nuclear volumes in subjects with schizophrenia. Am J Psychiatry 2002;159:59–65.
2. Henderson JM, Carpenter K, Cartwright H, Halliday GM. Loss of thalamic intralaminar nuclei in progressive supranuclear palsy and Parkinson's disease: clinical and therapeutic implications. Brain 2000;123 (Pt 7):1410–1421.
3. Moisset X, Bouhassira D. Brain imaging of neuropathic pain. NeuroImage 2007;37 (Suppl 1):S80–S88.
4. Popken GJ, Bunney WE, Potkin SG, Jones EG. Subnucleus-specific loss of neurons in medial thalamus of schizophrenics. Proc Natl Acad Sci USA 2000;97:9276–9280.
5. Benabid AL, Pollak P, Gervason C, Hoffmann D, Gao DM, Hommel M, Perret JE, de Rougemont J. Long-term suppression of tremor by chronic stimulation of the ventral intermediate thalamic nucleus. Lancet 1991;337:403–406.
6. Bittar RG, Kar-Purkayastha I, Owen SL, Bear RE, Green A, Wang S, Aziz TZ. Deep brain stimulation for pain relief: a meta-analysis. J Clin Neurosci 2005;12:515–519.
7. Lemaire JJ, Coste J, Ouchchane L, Caire F, Nuti C, Derost P, Cristini V, Gabrillargues J, Hemm S, Durif F, Chazal J. Brain mapping in stereotactic surgery: a brief overview from the probabilistic targeting to the patient-based anatomic mapping. NeuroImage 2007;37 (Suppl 1):S109–S115.
8. Patel NK, Khan S, Gill SS. Comparison of atlas- and magnetic-resonance-imaging-based stereotactic targeting of the subthalamic nucleus in the surgical treatment of Parkinson's disease. Stereotact Funct Neurosurg 2008;86:153–161.
9. Deoni SC, Rutt BK, Parrent AG, Peters TM. Segmentation of thalamic nuclei using a modified k-means clustering algorithm and high-resolution quantitative magnetic resonance imaging at 1.5 T. NeuroImage 2007;34:117–126.
10. Elolf E, Bockermann V, Gringel T, Knauth M, Dechent P, Helms G. Improved visibility of the subthalamic nucleus on high-resolution stereotactic MR imaging by added susceptibility (T2*) contrast using multiple gradient echoes. Am J Neuroradiol 2007;28:1093–1094.

11. Gringel T, Schulz-Schaeffer W, Elolf E, Frölich A, Dechent P, Helms G. Optimized high-resolution mapping of magnetization transfer (MT) at 3 Tesla for direct visualization of substructures of the human thalamus in clinically feasible measurement time. J Magn Reson Imaging 2009;29:1285–1292.
12. Morel A, Magnin M, Jeanmonod D. Multiarchitectonic and stereotactic atlas of the human thalamus. J Comp Neurol 1997;387:588–630.
13. Basser J, Mattiello J, Bihan DL. Estimation of the effective self-diffusion tensor from the NMR spin echo. J Magn Reson Ser B 1994;103:247–254.
14. Kingsley PB. Introduction to diffusion tensor imaging mathematics: Part II. Tensor calculations, noise, simulations and optimization. Concept Magnetic Reson Part A 2006;28:123–154.
15. Behrens TEJ, Woolrich MW, Jenkinson M, Johansen-Berg H, Nunes RG, Clare S, Matthews PM, Brandy JM, Smith SM. Characterization and propagation of uncertainty in diffusion-weighted MR imaging. Magn Reson Med 2003;50:1077–1088.
16. Jbabdi S, Woolrich MW, Behrens TEJ. Multiple-subjects connectivity-based parcelation using hierarchical dirichlet process mixture models. NeuroImage 2009;44:373–384.
17. Johansen-Berg H, Behrens TE, Sillery E, Ciccarelli O, Thompson AJ, Smith SM, Matthews PM. Functional-anatomical validation and individual variation of diffusion tractography-based segmentation of the human thalamus. Cereb Cortex 2005;15:31–39.
18. Unrath A, Klose U, Grodd W, Ludolph AC, Kassubek J. Directional colour encoding of the human thalamus by diffusion tensor imaging. Neurosci Lett 2008;434:322–327.
19. Wiegell MR, Tuch DS, Larsson HB, Wedeen VJ. Automatic segmentation of thalamic nuclei from diffusion tensor magnetic resonance imaging. NeuroImage 2003;19:391–401.
20. Ziyan U, Tuch DS, Westin CF. Segmentation of thalamic nuclei from DTI using spectral clustering. Med Image Comput Comput Assist Interv 2006;9:807–814.
21. Ziyan U, Westin CF. Joint segmentation of thalamic nuclei from a population of diffusion tensor MR images. Med Image Comput Comput Assist Interv 2008;11:279–286.
22. FMRIB Analysis Group. FSL. Oxford University: UK, 2007.
23. Alexander DC, Pierpaoli C, Basser PJ, Gee JC. Spatial transformations of diffusion tensor magnetic resonance images. IEEE Trans Med Imag 2001;20:1131–1139.
24. Leemans A, Jones DK. The B-matrix must be rotated when correcting for subject motion in DTI data. Magn Reson Med 2009;61:1336–1349.
25. Rohde GK, Barnett AS, Basser PJ, Marenco S, Pierpaoli C. Comprehensive approach for correction of motion and distortion in diffusion-weighted MRI. Magn Reson Med 2004;51:103–114.
26. Cook PA, Bai Y, Nedjati-Gilani S, Seunarine M, Hall MG, Parker GJ, Alexander DC. Camino: open-source diffusion-MRI reconstruction and processing. In 14th ISMRM Meeting, Seattle, Washington, USA. 2006; 2759.
27. Mang SC, Klose U, Reiterer S, Grodd W. Stability of diffusion direction based thalamus segmentation. In 17th Annual Meeting of the ISMRM, Honolulu, Hawaii, USA. 2009; 1456.
28. Demiralp C, Hughes JF, Laidlaw DH. Coloring 3D line fields using Boy's real projective plane immersion. IEEE Trans Vis Comput Graph 2009;15:1457–1463.
29. Basser PJ, Pajevic S, Pierpaoli C, Duda J, Aldroubi A. In vivo fiber tractography using DT-MRI data. Magn Reson Imaging 2000;44:625–632.
30. Basser PJ, Pajevic S. Method to reduce eigenvalue sorting bias in DT-MRI. In 7th Annual Meeting of the ISMRM, Philadelphia, Pennsylvania, USA. 1999; 1788.
31. Parker GJ, Schnabel JA, Symms MR, Werring DJ, Barker GJ. Nonlinear smoothing for reduction of systematic and random errors in diffusion tensor imaging. J Magn Reson Imaging 2000;11:702–710.
32. Behrens TEJ, Johansen-Berg H, Woolrich MW, Smith SM, Wheeler-Kingshott CAM, Boulby PA, Barker GJ, Sillery EL, Sheehan K, Ciccarelli O, Thompson AJ, Brady JM, Matthews PM. Non-invasive mapping of connections between human thalamus and cortex using diffusion imaging. Nat Neurosci 2003;6:750–757.